



## Article

# Nanoscale Multidimensional Pd/TiO<sub>2</sub>/g-C<sub>3</sub>N<sub>4</sub> Catalyst for Efficient Solar-Driven Photocatalytic Hydrogen Production

Ting-Han Lin <sup>1</sup>, Yin-Hsuan Chang <sup>1</sup>, Kuo-Ping Chiang <sup>1,2</sup>, Jer-Chyi Wang <sup>3,4,\*</sup>  and Ming-Chung Wu <sup>1,2,5,\*</sup> 

<sup>1</sup> Department of Chemical and Materials Engineering, College of Engineering, Chang Gung University, Taoyuan 33302, Taiwan; cgu.tinghanlin@gmail.com (T.-H.L.); cgu.yinhhsuanchang@gmail.com (Y.-H.C.); cgu.kuopingchiang@gmail.com (K.-P.C.)

<sup>2</sup> Green Technology Research Center, Chang Gung University, Taoyuan 33302, Taiwan

<sup>3</sup> Department of Electronic Engineering, College of Engineering, Chang Gung University, Taoyuan 33302, Taiwan

<sup>4</sup> Department of Neurosurgery, Chang Gung Memorial Hospital, Linkou, Taoyuan 33305, Taiwan

<sup>5</sup> Division of Neonatology, Department of Pediatrics, Chang Gung Memorial Hospital, Linkou, Taoyuan 33305, Taiwan

\* Correspondence: jcwang@mail.cgu.edu.tw (J.-C.W.); mingchungwu@cgu.edu.tw (M.-C.W.); Tel.: +886-32118800 (ext. 5784) (J.-C.W.); +886-32118800 (ext. 3834) (M.-C.W.)

**Abstract:** Solar-to-fuel conversion is an innovative concept for green energy, attracting many researchers to explore them. Solar-driven photocatalysts have become an essential solution to provide valuable chemicals like hydrogen, hydrocarbon, and ammonia. For sustainable stability under solar irradiation, titanium dioxide is regarded as an acceptable candidate, further showing excellent photocatalytic activity. Incorporating the photo-sensitizers, including noble metal nanoparticles and polymeric carbon-based material, can improve its photoresponse and facilitate the electron transfer and collection. In this study, we synthesized the graphitic carbon nitride (g-C<sub>3</sub>N<sub>4</sub>) nanosheet incorporated with high crystalline TiO<sub>2</sub> nanofibers (NF) as 1D/2D heterostructure catalyst for photocatalytic water splitting. The microstructure, optical absorption, crystal structure, charge carrier dynamics, and specific surface area were characterized systematically. The low bandgap of 2D g-C<sub>3</sub>N<sub>4</sub> nanosheets (NS) as a sensitizer improves the specific surface area and photo-response in the visible region as the incorporated amount increases. Because of the band structure difference between TiO<sub>2</sub> and g-C<sub>3</sub>N<sub>4</sub>, constructing the heterojunction formation, the superior separation of electron-hole is observed. The detection of reactive oxygen species and photo-assisted Kelvin probe microscopy are conducted to investigate the possible charge migration. The highest photocatalytic hydrogen production rate of Pd/TiO<sub>2</sub>/g-C<sub>3</sub>N<sub>4</sub> achieves 11.62 mmol·h<sup>−1</sup>·g<sup>−1</sup> under xenon lamp irradiation.

**Keywords:** TiO<sub>2</sub> nanofibers; g-C<sub>3</sub>N<sub>4</sub> nanosheets; heterostructure; photocatalyst; water splitting



**Citation:** Lin, T.-H.; Chang, Y.-H.; Chiang, K.-P.; Wang, J.-C.; Wu, M.-C. Nanoscale Multidimensional Pd/TiO<sub>2</sub>/g-C<sub>3</sub>N<sub>4</sub> Catalyst for Efficient Solar-Driven Photocatalytic Hydrogen Production. *Catalysts* **2021**, *11*, 59. <https://doi.org/10.3390/catal11010059>

Received: 4 December 2020

Accepted: 28 December 2020

Published: 4 January 2021

**Publisher's Note:** MDPI stays neutral with regard to jurisdictional claims in published maps and institutional affiliations.



**Copyright:** © 2021 by the authors. Licensee MDPI, Basel, Switzerland. This article is an open access article distributed under the terms and conditions of the Creative Commons Attribution (CC BY) license (<https://creativecommons.org/licenses/by/4.0/>).

## 1. Introduction

The depletion of energy resources and growing environmental concerns due to the expanding world population have invigorated efforts to exploit alternative clean energy. Photocatalytic hydrogen production as an attractive approach for resolving energy and environmental issues has received unprecedented attention [1,2]. Since the sun is virtually inexhaustible, photocatalysis can keep converting solar energy into hydrogen fuel during the day. Furthermore, the photocatalyst is indispensable for solving the environmental issue as for its degradation and antibacterial capability. However, the photocatalytic efficiency is still limited because of the rapid recombination of photocarrier. The significant improvement of heterostructure construction for photocatalytic water-splitting further attracts much attention, studying interfacial engineering [3].

Among the several metal oxides, titanium dioxide (TiO<sub>2</sub>) has been seen as potential material according to its reasonable cost, nontoxicity, high stability, and eco-friendliness. TiO<sub>2</sub> also shows excellent photocatalytic activity and photostability [4]. Therefore, many

studies are devoted to  $\text{TiO}_2$  photocatalyst for photodegradation of organic pollutants [5], photocatalytic hydrogen production [6], and photo-reduction  $\text{CO}_2$  [7]. However, there are many obstacles on the road for obtaining high efficiencies  $\text{TiO}_2$  photocatalysts, such as narrow spectral response interval and high recombination rate of hole and electron. Thus, numerous studies have been devoted to overcoming these problems, such as surface modification [8,9], fabricated heterojunction [10,11], multidimensional structure [12,13].

A variety of dimensional structures, 0D, 1D, and 2D materials, have been employed to design the multidimensional photocatalyst. For 0D/1D heterojunction materials, the quantum effect can effectively activate and convert the  $\text{H}_2\text{O}$  molecule. The inherent advantages of 1D material, high specific surface area, great exposed edge sites, and fast and long-distance electron transport can promote the charge separation. Therefore, the synergistic effect between 0D/1D material can remarkably enhance  $\text{H}_2$  evolution activity [14,15]. The emerging 1D/2D heterojunction materials also draw ever-growing research attention in the photocatalysis field. For designing the 2D nanomaterials, thin sheets or layers possess a significant number of active sites on the surface, a short diffusion pathway for facilitating excitons dissociation, superior electron mobility, and excellent catalyst supports ability [16,17]. Combined with the aforementioned advantages, 1D/2D heterojunction materials demonstrate rapid carrier transfer along the axial direction, restrain photocorrosion and agglomeration, prolonging the stability, and provide intimate interfaces between 1D/2D, favoring their versatility [18–20].

Graphitic carbon nitride ( $\text{g-C}_3\text{N}_4$ ) as a 2D material has been highlighted as a promising metal-free photocatalyst because of its unique electrical, optical, structural, and physicochemical properties [21–23].  $\text{g-C}_3\text{N}_4$  is a visible-light-driven photocatalyst ( $E_g \sim 2.7$  eV) with a conduction band edge at  $-1.1$  eV and valence band edge at  $1.6$  eV (vs. normal hydrogen electrode (NHE)). These fascinating properties allow  $\text{g-C}_3\text{N}_4$  to be used in photodegradation [24],  $\text{CO}_2$  photoreduction [25], water splitting [26,27], etc. Though  $\text{g-C}_3\text{N}_4$  possesses remarkable properties, its low absorption coefficient and high charge carriers recombination still limit  $\text{g-C}_3\text{N}_4$  performance. To overcome these drawbacks, forming a composite material with other semiconductors is a good strategy. Li et al. summarized recently advanced in  $\text{g-C}_3\text{N}_4$ -based heterojunction photocatalysts [28]. To date,  $\text{TiO}_2$  [29],  $\text{CdS}$  [30,31],  $\text{ZnIn}_2\text{S}_4$  [32],  $\text{BiO}(\text{COOH})$  [33],  $\text{MoS}_2$  [34,35], etc., have all been attempted to construct heterojunction  $\text{g-C}_3\text{N}_4$ -based heterojunction photocatalysts. 2D/1D nanostructured  $\text{g-C}_3\text{N}_4/\text{ZnO}$  demonstrates the formation of heterojunction effectively separates the charge carriers and thus enhances the photocatalytic activity [36]. 2D/1D nanostructured  $\text{g-C}_3\text{N}_4/\text{TiO}_2$  shows improved visible-light-driven photocatalytic activity and prolonged charge carrier lifetime [37,38].

Herein, we proposed a multidimensional heterostructure constructed by 2D  $\text{g-C}_3\text{N}_4$  nanosheet incorporated with high crystalline 1D  $\text{TiO}_2$  nanofibers for the photocatalytic degradation and water splitting. To achieve superior hydrogen production yield, we also introduced 0D Pd NP as cocatalyst, enriching the active site and rectifying the carrier transport in the interface by Schottky junction. The morphology, optical absorption, crystal structure, composition, and specific surface area were characterized systematically. The charge transfer behavior was unveiled by using a photo-assisted kelvin probe microscope. The superior separation of electron-hole was attributed to the heterojunction formation, and the preferred transfer of  $\text{TiO}_2$  and  $\text{g-C}_3\text{N}_4$  was interpreted. The nanoscale multidimensional Pd/ $\text{TiO}_2$ / $\text{g-C}_3\text{N}_4$  catalyst showed a high hydrogen evolution rate and presented the great potential to address the environment and energy issue in the future.

## 2. Results and Discussion

Multidimensional photocatalysts usually construct the heterostructure, then performing diverse crystal structure. To unveil the incorporation of  $\text{g-C}_3\text{N}_4$  NS and  $\text{TiO}_2$  NF, we studied their crystal structure using the synchrotron X-ray spectroscopy, with a radiative wavelength of  $1.025 \text{ \AA}$ . In Figure 1a, the typical peak at the  $2\theta$  of  $16.5^\circ$  was indexed to (101) plane of the reflection of anatase phase  $\text{TiO}_2$ . Among various  $\text{g-C}_3\text{N}_4/\text{TiO}_2$  cata-

lysts, the reflection of anatase  $\text{TiO}_2$  phase presented high intensity, indicating the perfect crystalline dominated by high crystalline  $\text{TiO}_2$  NF. The related crystallite size of anatase  $\text{TiO}_2$  in various  $\text{TiO}_2$  catalyst are all close to 34 nm, as reported in Table S1. Bulk  $\text{g-C}_3\text{N}_4$  shows two diffraction peaks at  $8.50^\circ$  and  $18.35^\circ$ , assigned to the in-plane arrangement and out-of-plane of C-N atoms in heptazine. Both diffraction peaks were hardly observed in a series of  $\text{g-C}_3\text{N}_4/\text{TiO}_2$  catalysts. For the better resolution and detailed inspection of crystal structure examination, we further collected the magnified spectra with a slower scan rate of  $0.005^\circ \text{ s}^{-1}$ . In Figure 1b, we observed the diffraction peak of (002) plane of  $\text{g-C}_3\text{N}_4$  NS appearing gradually as the incorporation concentration increased. Interestingly, the Raman spectra of various  $\text{g-C}_3\text{N}_4/\text{TiO}_2$  catalysts revealed a strong but broad peak, which becomes strong at Raman shift ranging from 1200 to  $1800 \text{ cm}^{-1}$ . It further covered the typical vibration modes of anatase  $\text{TiO}_2$ , including  $E_g$  ( $144 \text{ cm}^{-1}$ ),  $B_{1g}$  ( $397.9 \text{ cm}^{-1}$ ),  $A_{1g}$  ( $513.0 \text{ cm}^{-1}$ ), and  $E_g$  ( $637.2 \text{ cm}^{-1}$ ) [39]. These results indicated that the expected scattering of  $\text{g-C}_3\text{N}_4$  NS coupled with incident light significantly improved the successful incorporation of  $\text{g-C}_3\text{N}_4$  NS and  $\text{TiO}_2$  NF. Moreover, the evidence elaborated that the weak diffraction peak of (002) plane could speculate the laminate structure destruction by  $\text{TiO}_2$  NF embedded and layer disintegration.

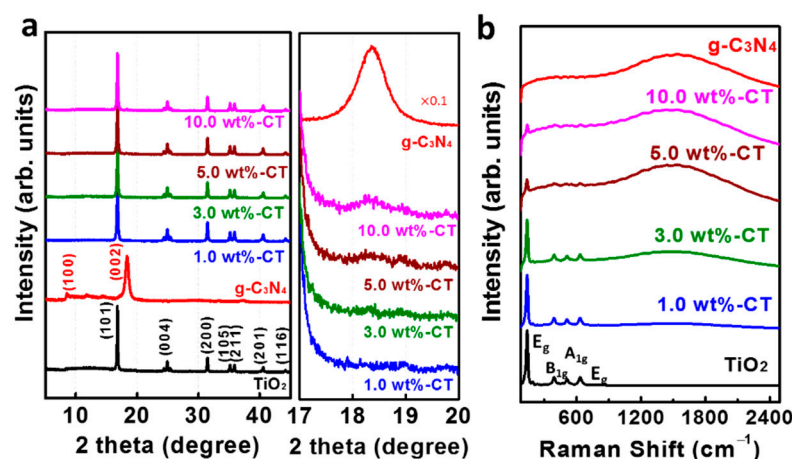


**Figure 1.** (a) Synchrotron X-ray spectra and (b) Raman spectra of the various  $\text{g-C}_3\text{N}_4/\text{TiO}_2$  catalysts.

To elucidate the chemical structure of  $\text{g-C}_3\text{N}_4/\text{TiO}_2$  catalysts, we further studied the FTIR spectra, as shown in Figure 2. The peaks at  $3300 \text{ cm}^{-1}$  and  $1200\text{--}1700 \text{ cm}^{-1}$  were assigned to N-H and C-N stretching vibration. N breathing mode of heptazine appeared at  $980 \text{ cm}^{-1}$ . The out-of-plane and in-plane bending vibration were indicated at  $810 \text{ cm}^{-1}$  and  $690 \text{ cm}^{-1}$ , respectively [40]. We found that the peak at low wavenumbers might be assigned to the  $E_g$  band ( $144 \text{ cm}^{-1}$ ) of anatase  $\text{TiO}_2$  because of the approximated energy difference of the photon between infrared absorption and Raman scattering. Obviously, with increasing amounts of  $\text{g-C}_3\text{N}_4$  NS, the stretching vibrations became stronger.

The optical properties are crucial factors for the photocatalytic activity. Pristine  $\text{g-C}_3\text{N}_4$  revealed an absorption peak at around 380 nm, attributed to the  $\pi\text{-}\pi^*$  transition in the aromatics. Incorporating  $\text{g-C}_3\text{N}_4$  with  $\text{TiO}_2$  NF substantially improved the absorption of the composite photocatalyst in the visible region. We found a red-shift appeared in the absorbance spectra and became intensive with increasing the  $\text{g-C}_3\text{N}_4$  amount (Figure 3a). It also was predictable to promote the overall activity of  $\text{g-C}_3\text{N}_4/\text{TiO}_2$  catalysts. The PL spectra are presented in Figure 3b; PL intensities were enhanced by incorporating  $\text{g-C}_3\text{N}_4$  NS because of the strong emission by  $\text{g-C}_3\text{N}_4$  NS. A slight red-shift was observed, being consistent with the absorption behavior. Notably, the board peak containing the second shoulder was attributed to the indirect radiative caused by a few structural defects trapping electrons in the in-plane  $\text{g-C}_3\text{N}_4$  [41]. As incorporated with  $\text{TiO}_2$  forming a heterostructure, it might provide an available pathway for excited charge carriers migration.

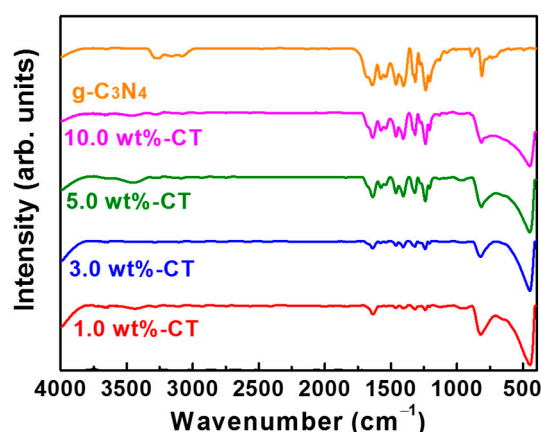


Figure 2. FTIR spectra of various g-C<sub>3</sub>N<sub>4</sub>/TiO<sub>2</sub> catalysts.

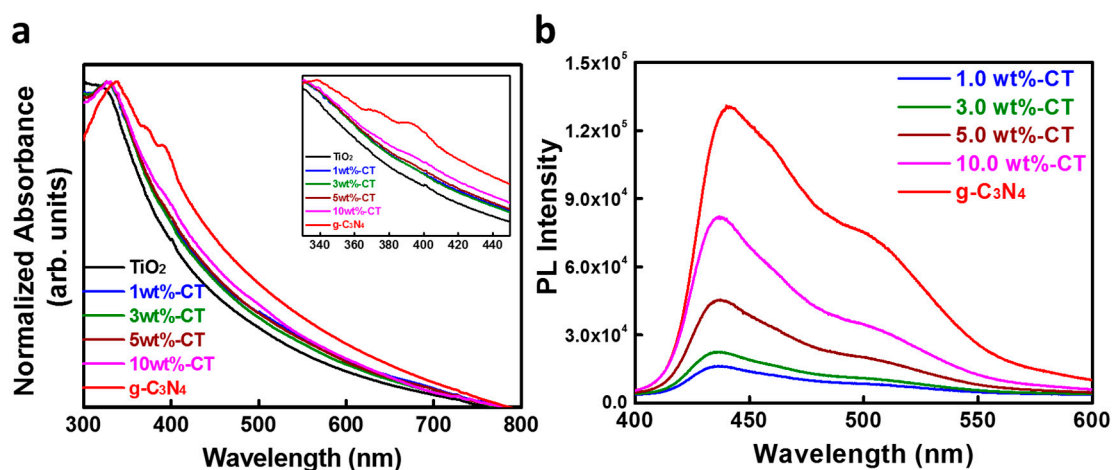


Figure 3. Optical properties of various g-C<sub>3</sub>N<sub>4</sub>/TiO<sub>2</sub> catalysts; (a) absorbance spectra; and (b) PL spectra.

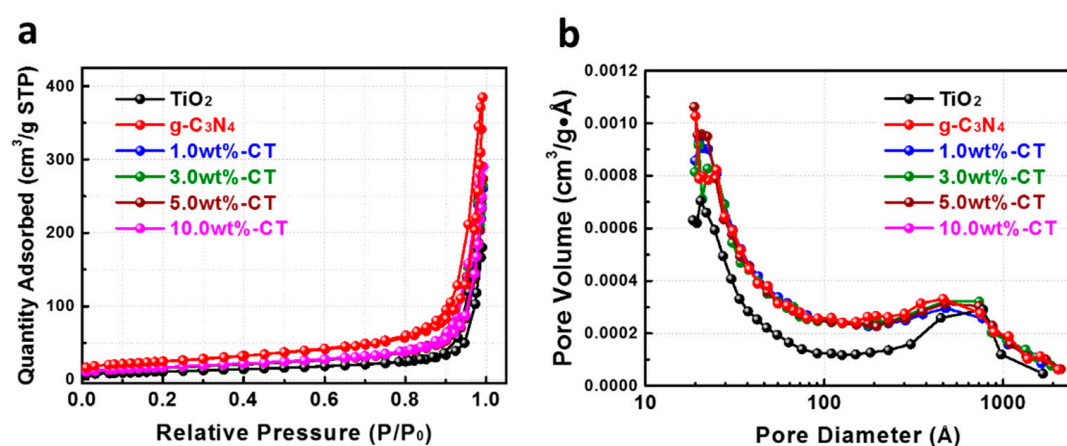
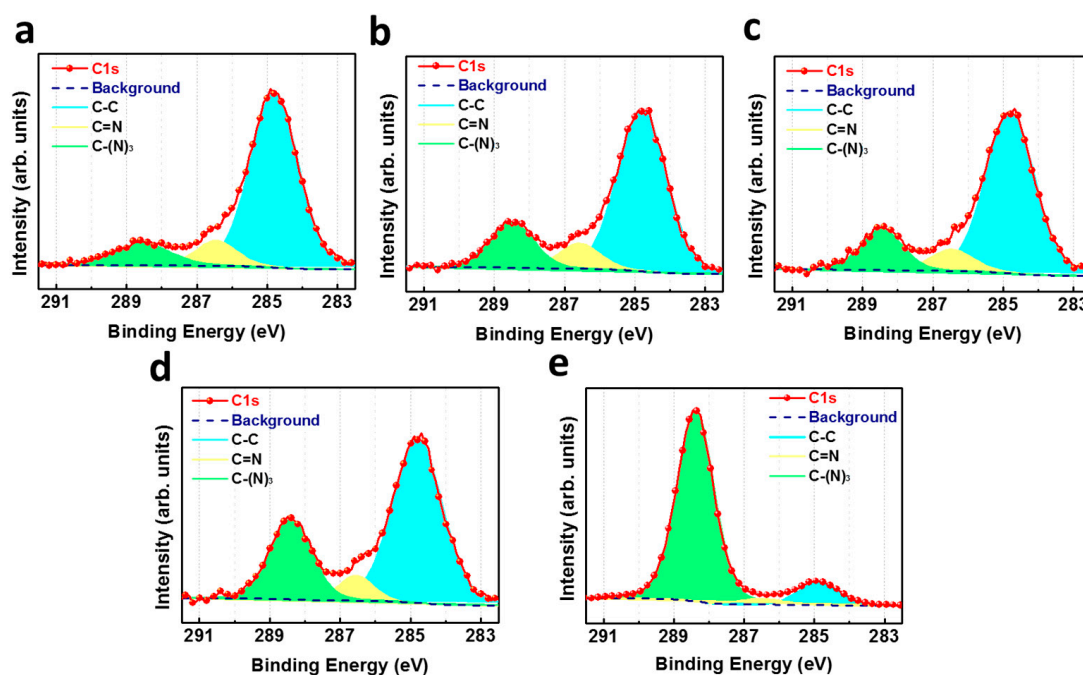
Two-dimensional g-C<sub>3</sub>N<sub>4</sub> NS with the ultrathin structure constructed by few layers usually shows a high specific surface area, providing rich active sites on the photocatalyst surface compared to one-dimensional photocatalysts. Hence, we examined the surface features of g-C<sub>3</sub>N<sub>4</sub>/TiO<sub>2</sub> catalysts by the Brunauer–Emmett–Teller (BET) and Barrett–Joyner–Halenda (BJH) method. The g-C<sub>3</sub>N<sub>4</sub> NS shows the remarkable properties in  $S_{\text{BET}}$  and pore features. The  $S_{\text{BET}}$  of g-C<sub>3</sub>N<sub>4</sub> NS is about  $88.9 \text{ m}^2 \cdot \text{g}^{-1}$ , and much higher than that of TiO<sub>2</sub> NF ( $49.6 \text{ m}^2 \cdot \text{g}^{-1}$ ), as shown in Table 1. When the incorporation amount of g-C<sub>3</sub>N<sub>4</sub> NS increased from 1.0 wt% to 10.0 wt%, the surface area of composites was gradually enhanced (Figure 4). At the same time, the BJH pore size and volume of g-C<sub>3</sub>N<sub>4</sub>/TiO<sub>2</sub> catalysts were also amplified, inferring the cavities or tunnels were constructed in g-C<sub>3</sub>N<sub>4</sub>/TiO<sub>2</sub> catalyst. It might be beneficial to aqueous penetration in the photocatalytic reaction.

To obtain the elemental composition, we implemented the X-ray photoelectron spectroscopy to analyze the C1s orbital. The typical C–C bonding presented in all of the g-C<sub>3</sub>N<sub>4</sub>/TiO<sub>2</sub> catalysts was assigned to the binding energy of 284.8 eV, suggesting the surface adsorption of carbon contamination and carbon dioxide (Figure 5). A low peak located at 286.6 eV was attributed to the C=N group [42]. Notably, we observed the increasing peak located at 288.6 eV referred to the C–N group, denoting the incorporation amount of g-C<sub>3</sub>N<sub>4</sub> increased in the g-C<sub>3</sub>N<sub>4</sub>/TiO<sub>2</sub> catalyst. We also studied their composition change by calculating the N/Ti and N/C atomic ratio, as reported in Table S2. Both ratios indicated the same tendency that the ratio of nitrogen to titanium and carbon increased with the increasing amount of g-C<sub>3</sub>N<sub>4</sub>.



**Table 1.** BET specific surface area ( $S_{\text{BET}}$ ), pore size, and pore volume of various  $g\text{-C}_3\text{N}_4/\text{TiO}_2$  catalysts.

Sample Name	$S_{\text{BET}}$ ( $\text{m}^2\cdot\text{g}^{-1}$ )	Pore Size (nm)		Pore Volume ( $\text{cm}^3\cdot\text{g}^{-1}$ )	
		BJH Adsorption	BJH Desorption	BJH Adsorption	BJH Desorption
$\text{TiO}_2$	49.64	22.7	21.3	0.295	0.294
1.0 wt%-CT	58.96	25.9	24.5	0.405	0.404
3.0 wt%-CT	59.71	26.7	25.0	0.413	0.412
5.0 wt%-CT	59.91	26.8	25.1	0.426	0.425
10.0 wt%-CT	61.74	28.2	26.7	0.451	0.450
$g\text{-C}_3\text{N}_4$	88.98	25.9	24.1	0.599	0.597

**Figure 4.** (a) Nitrogen adsorption–desorption BET isotherm curves and (b) related pore distribution curves of various  $g\text{-C}_3\text{N}_4/\text{TiO}_2$  catalysts.**Figure 5.** XPS spectra for C 1s orbital of  $g\text{-C}_3\text{N}_4/\text{TiO}_2$  catalyst with various  $g\text{-C}_3\text{N}_4$  addition, (a) 1.0 wt% (b) 3.0 wt%, (c) 5.0 wt%, and (d) 10.0 wt%, and (e) pristine  $g\text{-C}_3\text{N}_4$ .

As mentioned above, the successful incorporation with the visible-driven g-C<sub>3</sub>N<sub>4</sub> NS significantly improved several crucial factors for photocatalytic reaction, such as optical absorption, surface area, and heterojunction construction. To comprehend the optimal incorporation of g-C<sub>3</sub>N<sub>4</sub> NS for the catalytic activities, we evaluated their photodegradation of organic dyes and photocatalytic hydrogen production. In the photodegradation of methyl orange (MO), the essential elements are rich reactive oxygen species (ROS), which are highly active in attacking the organic dye, leading to discoloration. The 2D/1D heterostructure of g-C<sub>3</sub>N<sub>4</sub>/TiO<sub>2</sub> catalyst provides an alternative approach for the charge carrier migration, inhibiting the recombination and promoting the photo-excited electron-hole pairs to produce ROS efficiently. Figure 6a presented the photodegradation activity using various g-C<sub>3</sub>N<sub>4</sub>/TiO<sub>2</sub> catalysts. Bulk g-C<sub>3</sub>N<sub>4</sub> showed lower activity compared to TiO<sub>2</sub> NF, which was attributed to low crystalline and structural defects in bulk g-C<sub>3</sub>N<sub>4</sub>. Notably, incorporating the visible-driven g-C<sub>3</sub>N<sub>4</sub> NS with TiO<sub>2</sub> NF enhanced the overall degradation activity, and its reaction rate constant was up to 0.0099 min<sup>−1</sup> as the amount added to 5.0 wt%. Up to 10.0 wt%, discoloration behavior was inhibited (Figure 6b). It indicates that much more g-C<sub>3</sub>N<sub>4</sub> might dominate the surface feature because of the significant enhancement of S<sub>BET</sub> and optical absorption, whereas influenced exposure of TiO<sub>2</sub> active sites, leading to low intrinsic activity. Likewise, under the Xe lamp irradiation, the photocatalytic hydrogen production presented the tendency as the g-C<sub>3</sub>N<sub>4</sub> amounts increased to 5.0 wt%, in which the hydrogen production rate was 11.62 mmol·h<sup>−1</sup>·g<sup>−1</sup> (Figure 6c,d). Here, Pd NP decorated by the wet-impregnation method assisted the electron collection on the surface for proton reduction to hydrogen. Based on our best knowledge, excellent ordering in highly crystalline TiO<sub>2</sub> NF retains the numbers of electron-hole pairs and avoids the recombination as irradiated. When Pd NP locates at the interface of a metal oxide such as TiO<sub>2</sub>, the Schottky barrier forms and facilitates electron rectification, not back to metal oxide as electron once passes through the interface [6]. Thus, the optimal 5.0 wt% g-C<sub>3</sub>N<sub>4</sub>/TiO<sub>2</sub> catalyst with sufficient active sites and efficient charge transfer revealed significant photocatalytic activities.

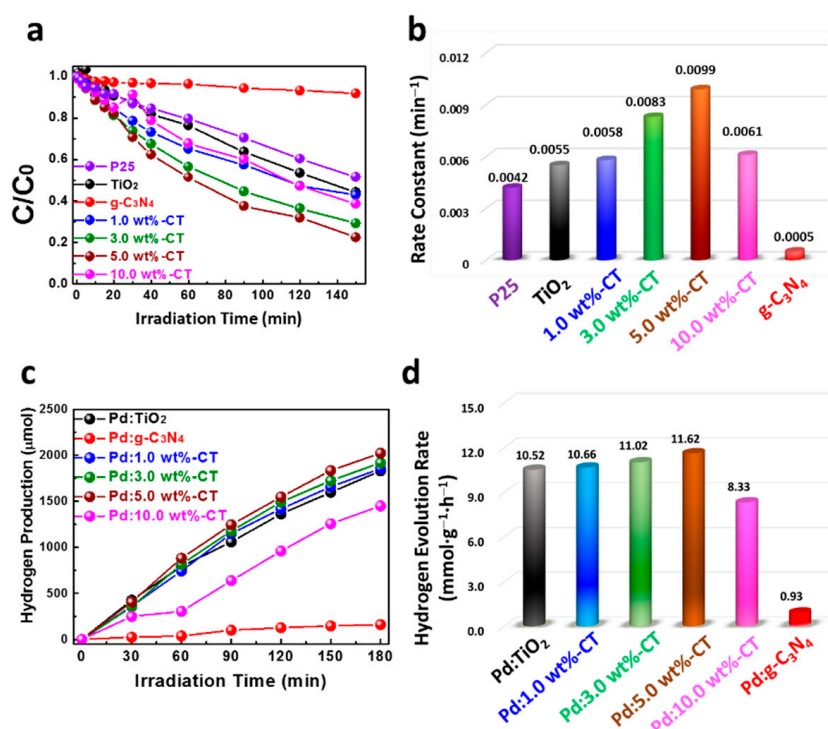


**Figure 6.** (a) Photodegradation of methyl orange and (b) the comparison chart of degradation rate; (c) photocatalytic hydrogen production and (d) the comparison chart of production rate.

We conducted the spherical-aberration corrected field-emission transmission electron microscope to investigate the heterostructure of Pd/TiO<sub>2</sub>/g-C<sub>3</sub>N<sub>4</sub> catalyst. Figure 7a revealed that TiO<sub>2</sub> NF lay on the multi-layer of g-C<sub>3</sub>N<sub>4</sub> NS and decorated with Pd NP. In the magnified image of g-C<sub>3</sub>N<sub>4</sub> NS (Figure 7b), it presented an ultrathin sheet morphology, implying the bulk g-C<sub>3</sub>N<sub>4</sub> was disintegrated by ultrasonic treatment. The topography was also reported in Figure S1, and the thickness is about 4.0 nm. In the case of TiO<sub>2</sub> NF (Figure 7c), a high ordering of anatase TiO<sub>2</sub> was observed, and the (101) plane with an interplanar spacing of 3.53 Å was referred to. (Figure 7d) Also, the Pd NP with a diameter of 3.0 nm was identified, and the typical (111) plane was observed, showing an interplanar spacing of 2.25 Å (Figure 7e).

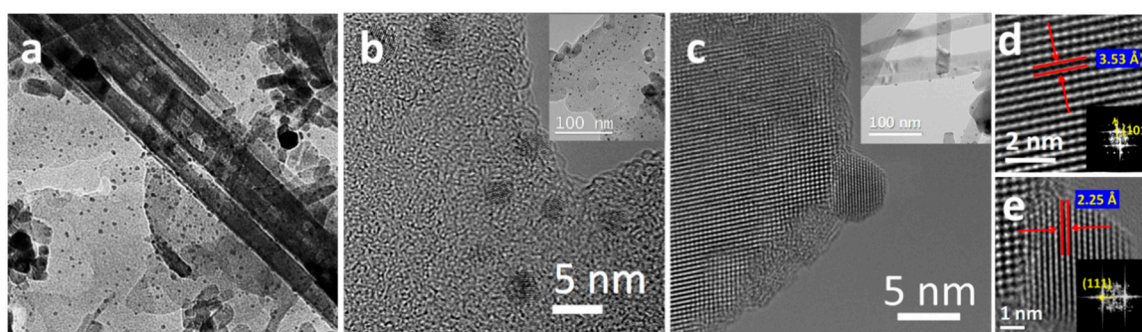


**Figure 7.** TEM images of (a) Pd/TiO<sub>2</sub>/g-C<sub>3</sub>N<sub>4</sub> catalyst; magnified images of (b) g-C<sub>3</sub>N<sub>4</sub> NS and (c) TiO<sub>2</sub> NF decorated with Pd NP; HRTEM images of (d) TiO<sub>2</sub> NF, and (e) Pd NP.

The scavengers were used to evaluate the reactive oxygen species (ROS) during the photodegradation to verify the charge transfer in the g-C<sub>3</sub>N<sub>4</sub>/TiO<sub>2</sub> catalyst's heterostructure. Tert-butyl alcohol (TBA) and *p*-benzoquinone (*p*-BQ) can investigate the role of relevant ROS, such as hydroxyl radical and superoxide radical, respectively. Ammonium oxalate (AO) can capture the hole that indirectly produces hydroxyl radical from the hydroxyl group. Figure 8a demonstrates the photodegradation using pristine TiO<sub>2</sub> NF. The addition of BQ or AO into the degradation reaction inhibited the TiO<sub>2</sub> activity. It elucidates the superoxide radicals derived by electrons and holes play a crucial role in the photodegradation. Similarly, a consistent phenomenon was observed in the photodegradation of g-C<sub>3</sub>N<sub>4</sub>/TiO<sub>2</sub> catalyst (Figure 8b). Notably, with the addition of TBA using TiO<sub>2</sub>, the discoloration by TiO<sub>2</sub> was still inhibited, implying a few hydroxyl radicals were produced. In contrast, g-C<sub>3</sub>N<sub>4</sub>/TiO<sub>2</sub> revealed good discoloration behavior, but the degradation rate of methyl orange was inhibited slightly with TBA, implying few hydroxyl radicals existed. Based on our best knowledge, the hydroxyl radical was produced by the reaction of the TiO<sub>2</sub>-induced hole and a hydroxyl group. Combining the g-C<sub>3</sub>N<sub>4</sub> NS, it provided the other pathway for the hole migration, indicating the change of the selectivity of hole which might migrate or react with the hydroxyl group on TiO<sub>2</sub>. Thus, the slight degradation activity can be attributed to the hole remaining on TiO<sub>2</sub>, which derived fewer hydroxyl radicals. We believed that most holes migrated from TiO<sub>2</sub> NF to g-C<sub>3</sub>N<sub>4</sub> NS, not producing hydroxyl radicals on the g-C<sub>3</sub>N<sub>4</sub> NS due to the inappropriate valance band position for hole-induced oxidation of the hydroxyl group. Herein, we proposed the charge transfer mechanism in the as-constructed heterostructure (Figure 8c). Under the Xe lamp irradiation, electron-hole pairs formed in both catalysts and then separated. The holes of TiO<sub>2</sub> NF prefer to transfer to the valance band of g-C<sub>3</sub>N<sub>4</sub> NS and combined with localized holes, directly oxidizing the organic dye or sacrificing agent. The electrons of TiO<sub>2</sub> retain in the conduction band. On the other hand, the electrons of g-C<sub>3</sub>N<sub>4</sub> transfer to the conduction band of TiO<sub>2</sub> NF and subsequently combine with local electrons to complete the photocatalytic degradation. Furthermore, as decorated Pd NP on the catalyst, electrons further passthrough the Schottky barrier and reduce protons to produce hydrogen.

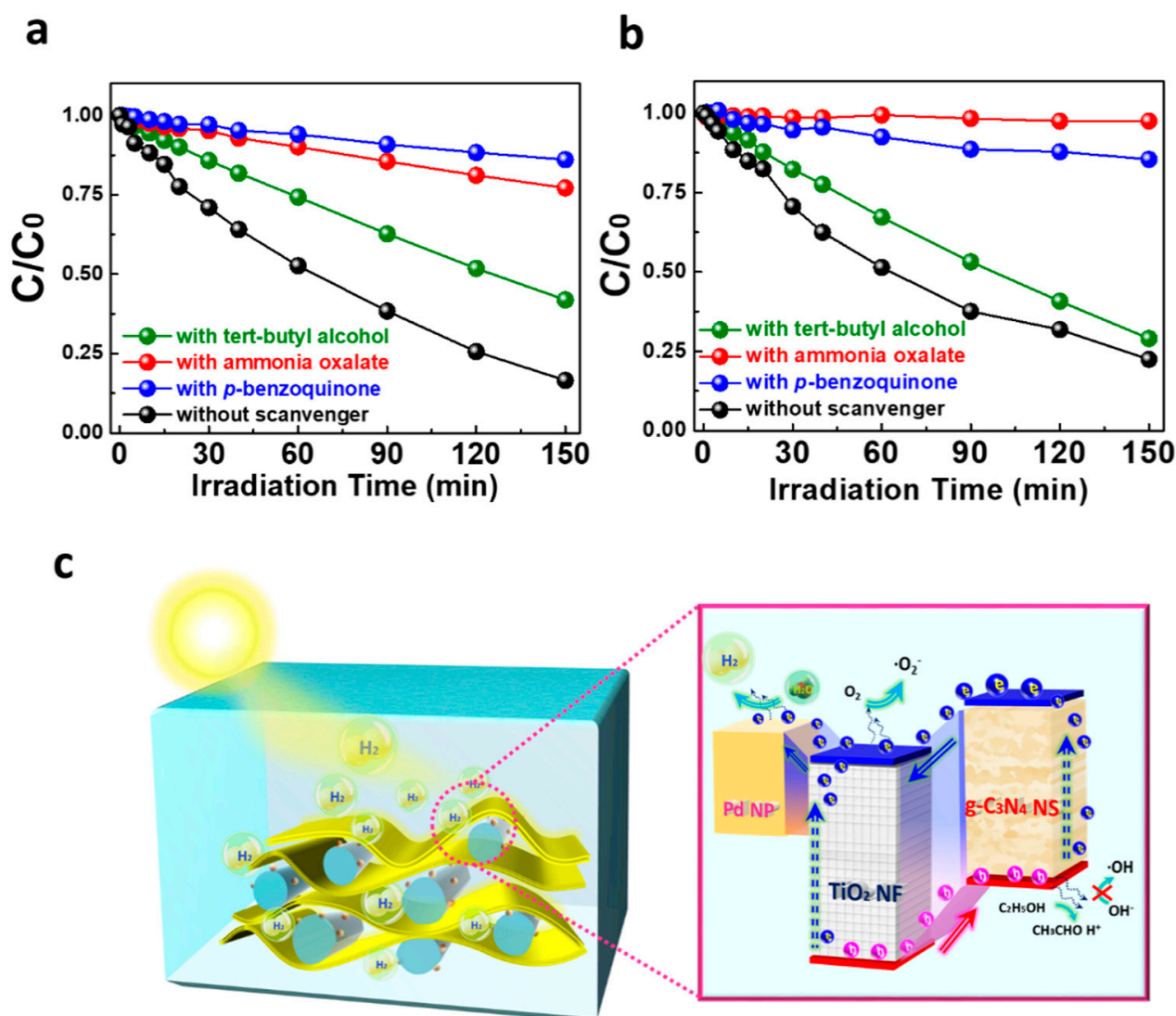


**Figure 8.** The photodegradation curves of (a) TiO<sub>2</sub> NF and (b) 5.0 wt% g-C<sub>3</sub>N<sub>4</sub>/TiO<sub>2</sub> catalyst toward the methyl orange with various scavengers, and (c) the scheme of the charge transfer mechanism.

To clarify the charge transfer in the heterostructure of g-C<sub>3</sub>N<sub>4</sub>/TiO<sub>2</sub>, we measured the surface potential and calculated the contact potential difference (CPD) with/without UV irradiation (Figure 9). The surface topographic images for TiO<sub>2</sub> NF and g-C<sub>3</sub>N<sub>4</sub> NS clearly observe the TiO<sub>2</sub> NF laid on g-C<sub>3</sub>N<sub>4</sub> NS in Figure 9a-1. We further conducted the surface potential mapping in this area. In dark (Figure 9a-2), both TiO<sub>2</sub> NF and g-C<sub>3</sub>N<sub>4</sub> NS presented similar CPD due to the successful construction of heterostructure, causing the Fermi level alignment. As UV irradiated to the g-C<sub>3</sub>N<sub>4</sub>/TiO<sub>2</sub> (Figure 9b-1), the surface potential of TiO<sub>2</sub> increased significantly instead of that of g-C<sub>3</sub>N<sub>4</sub> (Figure 9b-2). The slight increment of surface potential on g-C<sub>3</sub>N<sub>4</sub> (0.073 mV) suggested an overall Fermi level increase, indicating a positive work function shift (Figure 9c). It also indicated that the photo-induced electrons might migrate to TiO<sub>2</sub>, whose average potential change ( $\Delta P$ ) is about 0.263 V. A dramatic increment in potential which is observed in the interface between TiO<sub>2</sub> NF and g-C<sub>3</sub>N<sub>4</sub> NS implied electrons transfer. This result elucidated the g-C<sub>3</sub>N<sub>4</sub>/TiO<sub>2</sub> constructed with the type II heterojunction. The photo-assisted KPFM would help verify the heterojunctions and the charge migration in the multidimensional photocatalyst.



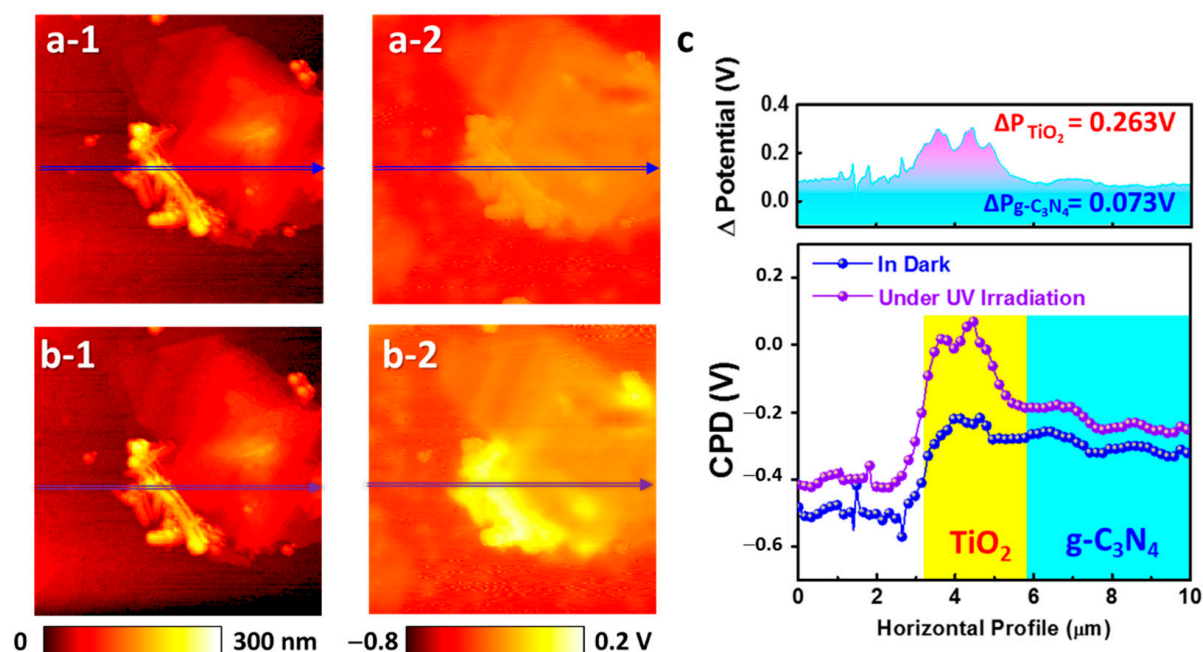


**Figure 9.** Topographic images of g-C<sub>3</sub>N<sub>4</sub>/TiO<sub>2</sub> catalyst (a-1) in dark, and (b-1) under UV irradiation; the surface potential images of g-C<sub>3</sub>N<sub>4</sub>/TiO<sub>2</sub> catalyst (a-2) in dark, and (b-2) under UV irradiation; (c) horizontal profile for the surface potential mapping of g-C<sub>3</sub>N<sub>4</sub>/TiO<sub>2</sub> catalyst, and related potential change (upper).

### 3. Materials and Methods

#### 3.1. Synthesis of Catalyst

Titanium dioxide nanofibers (TiO<sub>2</sub> NF) were prepared by the hydrothermal method and further calcined in the air, according to our previous work [43]. About 2.50 g anatase TiO<sub>2</sub> powder (Acros, 98%, Geel, Belgium) was gradually poured in 62.5 mL of 10.0 M NaOH (Fisher Scientific, >97%, Fair Lawn, NJ, USA) aqueous solution in a Teflon-lined autoclave. The mixture solution was vigorously agitated for 30 min, followed by heating to 150 °C for 24 h. Sodium titanate nanofibers were obtained and subsequently washed by diluted hydrochloric acid (HCl, Acros, 37%, Geel, Belgium) to eliminate sodium ions. Then, hydrogen titanate nanofibers was washed with distilled water until neutralized and then collected by filtration. Finally, the sample was dried at 80 °C in the oven. The highly crystalline TiO<sub>2</sub> NFs were obtained after the calcination of hydrogen titanate at 600 °C. On the other hand, bulk graphitic carbon nitride (g-C<sub>3</sub>N<sub>4</sub>) was synthesized by thermal polymerization at 550 °C. For the excellent dispersion in aqueous and the disintegration of bulk status, bulk g-C<sub>3</sub>N<sub>4</sub> was vigorously agitated in aqueous by ultrasonicator. To further obtain the g-C<sub>3</sub>N<sub>4</sub>/TiO<sub>2</sub> catalysts, 0.50 g TiO<sub>2</sub> NFs were suspended in 100.0 mL of DI water and subsequently irradiated under a UV-B lamp for activation of TiO<sub>2</sub>. Various amounts of g-C<sub>3</sub>N<sub>4</sub>, including 1.0, 3.0, 5.0, 10.0 wt%, were added into the solution and stirred for 30 min. After drying, various g-C<sub>3</sub>N<sub>4</sub>/TiO<sub>2</sub> catalysts were acquired and named as CT. For improving the hydrogen production ability, 1.0 wt% palladium nanoparticles were deposited on as-prepared catalysts by the wet-impregnation method. Palladium (II) acetate (Pd(OCOCH<sub>3</sub>)<sub>2</sub>, ACROS, 99.9%, Geel, Belgium) was dissolved in a mixture of ethanol and acetone with a volume ratio of 1:1. Then, 0.60 g g-C<sub>3</sub>N<sub>4</sub>/TiO<sub>2</sub> catalysts were further added to the solution and stirred for 3 h. After dried at 80 °C, remained powder was calcined at 350 °C for 3 h under the mixture flow of 15% H<sub>2</sub> in N<sub>2</sub> buffer. Finally, the multidimensional Pd/TiO<sub>2</sub>/g-C<sub>3</sub>N<sub>4</sub> catalyst was obtained.

### 3.2. Material Characterization

The crystal structures of various g-C<sub>3</sub>N<sub>4</sub>/TiO<sub>2</sub> catalysts were characterized by synchrotron X-ray spectroscopy ( $\lambda \sim 1.025$  Å) on beamline 13A1 of the National Synchrotron Radiation Research Center (NSRRC) in Taiwan. It was recorded from  $2\theta$  between 5 and 45 with a  $0.01^\circ$  step at  $0.05^\circ \text{ s}^{-1}$ . The magnified X-ray spectra were obtained from  $2\theta$  between 17.00 and 20.00 with a  $0.01^\circ$  step at  $0.005^\circ \text{ s}^{-1}$ . The chemical structure was analyzed using Fourier-transform infrared spectroscopy (FT-IR, Tensor 27, Bruker, Karlsruhe, Germany) in the range of 4000 to  $450 \text{ cm}^{-1}$  with a resolution of  $2.0 \text{ cm}^{-1}$ . In the absorbance characterization, catalyst powders were dispersed in the DI water and then placed in a quartz cuvette. The absorbance spectra were measured by UV-VIS spectrophotometer (V-730, JASCO, Tokyo, Japan). For the photoluminescence measurement, catalysts were squeezed as the pellet and determined by photoluminescence spectrophotometer (UniDron-TRPL, CL technology, New Taipei City, Taiwan) with an excitation of 375 nm laser. The surface feature of photocatalysts, including specific surface area, pore size, and pore volume, were investigated by surface area and porosity analyzer (ASAP 2020, Micromeritics, Norcross, GA, USA). The X-ray photoelectron spectrometer with an X-ray source of Al K $\alpha$  (K-alpha X-ray photoelectron spectrometer, Thermo Fisher Scientific, Waltham, MA, USA) was used to analyze the chemical state and precise composition. The morphology of Pd/TiO<sub>2</sub>/g-C<sub>3</sub>N<sub>4</sub> catalysts was observed by using the spherical-aberration corrected field-emission transmission electron microscope (JEM-ARM200FTH, JEOL, Tokyo, Japan).

### 3.3. Photocatalytic Experiment

We implemented two methods, including photodegradation of methyl orange (C<sub>6</sub>H<sub>4</sub>(OH)<sub>2</sub>, Acros, 99.5%, Geel, Belgium) and photocatalytic hydrogen production, to evaluate the photocatalytic activity of various g-C<sub>3</sub>N<sub>4</sub>/TiO<sub>2</sub> catalysts. In the former part, 20.0 mg of the catalyst was dispersed in the 10.0 ppm of methyl orange aqueous, further stirred for 60 min in the dark to lower the surface adsorption error. The suspension was then irradiated to two UV-B lamps (G8T5E 8W, SANKYO DENKI, Kanagawa, Japan) at ambient conditions under continuous stirring. The distance of lamps-to-reactor was kept about 5.0 cm. At the optimal time interval, we sampled about 3.0 mL of the suspension. Before the absorbance spectra examination, these samples were centrifuged for 15 min at 5000 rpm. The concentration of residue dye in the supernatant was estimated by using a UV-VIS spectrophotometer (V-730, JASCO, Tokyo, Japan) in the 400–900 nm, followed by recalculated from the calibration equation.

In the photocatalytic hydrogen production, the experiment was conducted in the Labsolar 6A system (Perfectlight Technology, Beijing, China) with a 300.0 mL glass reactor under 300 W Xenon irradiation. Total of 50.0 mg catalyst was dispersed in the 100.0 mL mixture of equivolume deionized water and ethanol. The hydrogen concentration was determined by online gas chromatography with a barrier ionization discharge detector (Shimadzu, Nexis GC-2030, with helium as a carrier gas, Kyoto, Japan) at a time interval of 30 min for 3 h.

For the investigation of different reactive oxygen species, we used the specific scavengers including *p*-benzoquinone (Acros, 99%, Geel, Belgium), ammonia oxalate (VETEC, 98%, trademark of Sigma-Aldrich, St. Louis, MO, USA), and tert-butyl alcohol (J.T.Baker,  $\geq 99.0\%$ , Phillipsburg, NJ, USA) in the photodegradation of 5.0 ppm methyl orange for the captivity of superoxide radicals, holes, and hydroxyl radicals.

## 4. Conclusions

Multidimensional Pd/TiO<sub>2</sub>/g-C<sub>3</sub>N<sub>4</sub> catalysts were fabricated for the photocatalytic hydrogen production under xenon lamp irradiation. Constructing the heterostructure of 2D g-C<sub>3</sub>N<sub>4</sub> NS and 1D TiO<sub>2</sub> NF can associate both advantages, such as the enhanced specific surface area, optical absorption in the visible region, and excellent charge transfer. The Pd NP decoration on the optimal g-C<sub>3</sub>N<sub>4</sub>/TiO<sub>2</sub> catalyst improved the overall hydrogen production up to  $11.62 \text{ mmol} \cdot \text{h}^{-1} \cdot \text{g}^{-1}$ . Through the ROS detection and KPFM investigation,

we clarified the charge transfer behavior belonged to type II heterojunction. The photo-induced electrons prefer to migrate from g-C<sub>3</sub>N<sub>4</sub> NS to TiO<sub>2</sub> NF, reducing proton for hydrogen evolution on Pd cocatalyst. It also contributed to the excellent and rational electron-holes separation, inhibiting the recombination. In summary, the 0D/1D/2D multidimensional Pd/TiO<sub>2</sub>/g-C<sub>3</sub>N<sub>4</sub> catalyst demonstrated excellent feasibility for the photocatalytic material design, also showing high activity under solar irradiation for solving the energy crisis and environmental concerns in the future.

**Supplementary Materials:** The following are available online at <https://www.mdpi.com/2073-4344/11/1/59/s1>, Figure S1: Surface topographic image of g-C<sub>3</sub>N<sub>4</sub> NS. Table S1: The calculated crystallite size of anatase TiO<sub>2</sub> in various catalysts. Table S2: The calculated atomic ratio.

**Author Contributions:** T.-H.L. and K.-P.C. performed the research and analyzed the data; T.-H.L. and Y.-H.C. wrote the paper. T.-H.L. and J.-C.W. revised the paper. M.-C.W. was the supervisor and revised the paper. All authors have read and agreed to the published version of the manuscript.

**Funding:** This research was funded by Ministry of Science and Technology, Taiwan, Project No. 106-2221-E-182-057-MY3, 108-2119-M-002-005, 109-2221-E-182-059, and 109-3116-F-002-002-CC2, Chang Gung University (QZRPD181) and Chang Gung Memorial Hospital, Linkou (CMRPD2H0163 and BMRPC74).

**Institutional Review Board Statement:** Not applicable.

**Informed Consent Statement:** Not applicable.

**Data Availability Statement:** The data presented in this study and supporting information are available.

**Acknowledgments:** The authors appreciate Ming-Tao Lee (BL-13A1) and Jyh-Fu Lee (BL-17C1) at National Synchrotron Radiation Research Centre for useful discussion and suggestions.

**Conflicts of Interest:** The authors declare no conflict of interest.

## References

- Chen, S.S.; Takata, T.; Domen, K. Particulate Photocatalysts for Overall Water Splitting. *Nat. Rev. Mater.* **2017**, *2*, 17. [CrossRef]
- Wang, Y.O.; Suzuki, H.; Xie, J.J.; Tomita, O.; Martin, D.J.; Higashi, M.; Kong, D.; Abe, R.; Tang, J.W. Mimicking Natural Photosynthesis: Solar to Renewable H<sub>2</sub> Fuel Synthesis by Z-scheme Water Splitting Systems. *Chem. Rev.* **2018**, *118*, 5201–5241. [CrossRef] [PubMed]
- Wang, Z.; Li, C.; Domen, K. Recent Developments in Heterogeneous Photocatalysts for Solar-driven Overall Water Splitting. *Chem. Soc. Rev.* **2019**, *48*, 2109–2125. [CrossRef] [PubMed]
- Kang, X.L.; Liu, S.H.; Dai, Z.D.; He, Y.P.; Song, X.Z.; Tan, Z.Q. Titanium Dioxide: From Engineering to Applications. *Catalysts* **2019**, *9*, 32. [CrossRef]
- Wu, M.C.; Lin, T.H.; Hsu, K.H.; Hsu, J.F. Photo-induced Disinfection Property and Photocatalytic Activity Based on the Synergistic Catalytic Technique of Ag Doped TiO<sub>2</sub> Nanofibers. *Appl. Surf. Sci.* **2019**, *484*, 326–334. [CrossRef]
- Wu, M.C.; Huang, W.K.; Lin, T.H.; Lu, Y.J. Photocatalytic Hydrogen Production and Photodegradation of Organic Dyes of Hydrogenated TiO<sub>2</sub> Nanofibers Decorated Metal Nanoparticles. *Appl. Surf. Sci.* **2019**, *469*, 34–43. [CrossRef]
- Xu, F.Y.; Zhang, J.J.; Zhu, B.C.; Yu, J.G.; Xu, J.S. CuInS<sub>2</sub> Sensitized TiO<sub>2</sub> Hybrid Nanofibers for Improved Photocatalytic CO<sub>2</sub> Reduction. *Appl. Catal. B Environ.* **2018**, *230*, 194–202. [CrossRef]
- Wu, M.C.; Hsiao, K.C.; Chang, Y.H.; Chan, S.H. Photocatalytic Hydrogen Evolution of Palladium Nanoparticles Decorated Black TiO<sub>2</sub> Calcined in Argon Atmosphere. *Appl. Surf. Sci.* **2018**, *430*, 407–414. [CrossRef]
- Yin, G.H.; Huang, X.Y.; Chen, T.Y.; Zhao, W.; Bi, Q.Y.; Xu, J.; Han, Y.F.; Huang, F.Q. Hydrogenated Blue Titania for Efficient Solar to Chemical Conversions: Preparation, Characterization, and Reaction Mechanism of CO<sub>2</sub> Reduction. *ACS Catal.* **2018**, *8*, 1009–1017. [CrossRef]
- Wu, M.C.; Hsiao, K.C.; Chang, Y.H.; Kordas, K. Core-shell Heterostructures of Rutile and Anatase TiO<sub>2</sub> Nanofibers for Photocatalytic Solar Energy Conversion. *ACS Appl. Nano Mater.* **2019**, *2*, 1970–1979. [CrossRef]
- Ansón-Casaos, A.; Hernández-Ferrer, J.; Vallan, L.; Xie, H.; Lira-Cantú, M.; Benito, A.M.; Maser, W.K. Functionalized Carbon Dots on TiO<sub>2</sub> for Perovskite Photovoltaics and Stable Photoanodes for Water Splitting. *Int. J. Hydrogen Energy* **2020**. [CrossRef]
- Geng, R.; Yin, J.J.; Zhou, J.X.; Jiao, T.F.; Feng, Y.; Zhang, L.X.; Chen, Y.; Bai, Z.H.; Peng, Q.M. In Situ Construction of Ag/TiO<sub>2</sub>/g-C<sub>3</sub>N<sub>4</sub> Heterojunction Nanocomposite Based on Hierarchical Co-assembly with Sustainable Hydrogen Evolution. *Nanomaterials* **2020**, *10*, 13. [CrossRef] [PubMed]
- Hernández-Ferrer, J.; Ansón-Casaos, A.; Víctor-Román, S.; Sanahuja-Parejo, O.; Martínez, M.T.; Villacampa, B.; Benito, A.M.; Maser, W.K. Photoactivity Improvement of TiO<sub>2</sub> Electrodes by Thin Hole Transport Layers of Reduced Graphene Oxide. *Electrochim. Acta* **2019**, *298*, 279–287. [CrossRef]

14. Chen, Q.H.; Zhang, M.M.; Li, J.Y.; Zhang, G.D.; Xin, Y.J.; Chai, C. Construction of Immobilized 0D/1D Heterostructure Photocatalyst Au/CuS/CdS/TiO<sub>2</sub> NBs with Enhanced Photocatalytic Activity towards Moxifloxacin Degradation. *Chem. Eng. J.* **2020**, *389*, 12. [\[CrossRef\]](#)
15. Wu, M.C.; Chen, C.H.; Huang, W.K.; Hsiao, K.C.; Lin, T.H.; Chan, S.H.; Wu, P.Y.; Lu, C.F.; Chang, Y.H.; Lin, T.F.; et al. Improved Solar-driven Photocatalytic Performance of Highly Crystalline Hydrogenated TiO<sub>2</sub> Nanofibers with Core-Shell Structure. *Sci. Rep.* **2017**, *7*, 12. [\[CrossRef\]](#)
16. Zhou, X.J.; Shao, C.L.; Li, X.H.; Wang, X.X.; Guo, X.H.; Liu, Y.C. Three Dimensional Hierarchical Heterostructures of g-C<sub>3</sub>N<sub>4</sub> Nanosheets/TiO<sub>2</sub> Nanofibers: Controllable Growth via Gas-solid Reaction and Enhanced Photocatalytic Activity under Visible Light. *J. Hazard. Mater.* **2018**, *344*, 113–122. [\[CrossRef\]](#)
17. Zhu, M.S.; Kim, S.; Mao, L.; Fujitsuka, M.; Zhang, J.Y.; Wang, X.C.; Majima, T. Metal-free Photocatalyst for H<sub>2</sub> Evolution in Visible to Near-infrared Region: Black Phosphorus/Graphitic Carbon Nitride. *J. Am. Chem. Soc.* **2017**, *139*, 13234–13242. [\[CrossRef\]](#)
18. Hao, R.R.; Wang, G.H.; Tang, H.; Sun, L.L.; Xu, C.; Han, D.Y. Template-free Preparation of Macro/Mesoporous g-C<sub>3</sub>N<sub>4</sub>/TiO<sub>2</sub> Heterojunction Photocatalysts with Enhanced Visible Light Photocatalytic Activity. *Appl. Catal. B Environ.* **2016**, *187*, 47–58. [\[CrossRef\]](#)
19. Tao, R.; Li, X.H.; Li, X.W.; Shao, C.L.; Liu, Y.C. TiO<sub>2</sub>/SrTiO<sub>3</sub>/g-C<sub>3</sub>N<sub>4</sub> Ternary Heterojunction Nanofibers: Gradient Energy Band, Cascade Charge Transfer, Enhanced Photocatalytic Hydrogen Evolution, and Nitrogen Fixation. *Nanoscale* **2020**, *12*, 8320–8329. [\[CrossRef\]](#)
20. Wang, C.J.; Zhao, Y.L.; Xu, H.; Li, Y.F.; Wei, Y.C.; Liu, J.; Zhao, Z. Efficient Z-scheme Photocatalysts of Ultrathin g-C<sub>3</sub>N<sub>4</sub>-wrapped Au/TiO<sub>2</sub>-Nanocrystals for Enhanced Visible-Light-Driven Conversion of CO<sub>2</sub> with H<sub>2</sub>O. *Appl. Catal. B Environ.* **2020**, *263*, 13. [\[CrossRef\]](#)
21. Fu, J.W.; Yu, J.G.; Jiang, C.J.; Cheng, B. g-C<sub>3</sub>N<sub>4</sub>-based Heterostructured Photocatalysts. *Adv. Energy Mater.* **2018**, *8*, 31. [\[CrossRef\]](#)
22. Kumar, S.; Karthikeyan, S.; Lee, A.F. g-C<sub>3</sub>N<sub>4</sub>-based Nanomaterials for Visible Light-Driven Photocatalysis. *Catalysts* **2018**, *8*, 47. [\[CrossRef\]](#)
23. Ong, W.J.; Tan, L.L.; Ng, Y.H.; Yong, S.T.; Chai, S.P. Graphitic carbon nitride (g-C<sub>3</sub>N<sub>4</sub>)-based Photocatalysts for Artificial Photosynthesis and Environmental Remediation: Are We A Step Closer to Achieving Sustainability? *Chem. Rev.* **2016**, *116*, 7159–7329. [\[CrossRef\]](#) [\[PubMed\]](#)
24. Xu, J.; Wang, Z.P.; Zhu, Y.F. Enhanced Visible-Light-Driven Photocatalytic Disinfection Performance and Organic Pollutant Degradation Activity of Porous g-C<sub>3</sub>N<sub>4</sub> Nanosheets. *ACS Appl. Mater. Interfaces* **2017**, *9*, 27727–27735. [\[CrossRef\]](#)
25. Ong, W.J. 2D/2D Graphitic Carbon Nitride (g-C<sub>3</sub>N<sub>4</sub>) Heterojunction Nanocomposites for Photocatalysis: Why Does Face-to-Face Interface Matter? *Front. Mater.* **2017**, *4*, 10. [\[CrossRef\]](#)
26. Mun, S.J.; Park, S.J. Graphitic Carbon Nitride Materials for Photocatalytic Hydrogen Production via Water Splitting: A Short Review. *Catalysts* **2019**, *9*, 17. [\[CrossRef\]](#)
27. Naseri, A.; Samadi, M.; Pourjavadi, A.; Moshfegh, A.Z.; Ramakrishna, S. Graphitic carbon nitride (g-C<sub>3</sub>N<sub>4</sub>)-based Photocatalysts for Solar Hydrogen Generation: Recent Advances and Future Development Directions. *J. Mater. Chem. A* **2017**, *5*, 23406–23433. [\[CrossRef\]](#)
28. Li, Y.; Zhou, M.; Cheng, B.; Shao, Y. Recent Advances in g-C<sub>3</sub>N<sub>4</sub>-based Heterojunction Photocatalysts. *J. Mater. Sci. Technol.* **2020**, *56*, 1–17. [\[CrossRef\]](#)
29. Zhu, Z.D.; Murugananthan, M.; Gu, J.; Zhang, Y.R. Fabrication of a Z-scheme g-C<sub>3</sub>N<sub>4</sub>/Fe-TiO<sub>2</sub> Photocatalytic Composite with Enhanced Photocatalytic Activity under Visible Light Irradiation. *Catalysts* **2018**, *8*, 16. [\[CrossRef\]](#)
30. Ji, C.; Du, C.; Steinkruger, J.D.; Zhou, C.; Yang, S.Y. In-situ Hydrothermal Fabrication of CdS/g-C<sub>3</sub>N<sub>4</sub> Nanocomposites for Enhanced Photocatalytic Water Splitting. *Mater. Lett.* **2019**, *240*, 128–131. [\[CrossRef\]](#)
31. Liu, X.M.; Liu, Y.; Zhang, W.K.; Zhong, Q.Y.; Ma, X.Y. In Situ Self-assembly of 3d Hierarchical 2D/2D CdS/g-C<sub>3</sub>N<sub>4</sub> Heterojunction with Excellent Photocatalytic Performance. *Mater. Sci. Semicond. Process* **2020**, *105*, 9. [\[CrossRef\]](#)
32. Lin, B.; Li, H.; An, H.; Hao, W.B.; Wei, J.J.; Dai, Y.Z.; Ma, C.S.; Yang, G.D. Preparation of 2D/2D g-C<sub>3</sub>N<sub>4</sub> Nanosheet@ZnIn<sub>2</sub>S<sub>4</sub> Nanoleaf Heterojunctions with Well-designed High-speed Charge Transfer Nanochannels towards High Efficiency Photocatalytic Hydrogen Evolution. *Appl. Catal. B Environ.* **2018**, *220*, 542–552. [\[CrossRef\]](#)
33. Cui, Y.Q.; Zhang, X.Y.; Zhang, H.X.; Cheng, Q.F.; Cheng, X.W. Construction of BiOOH/g-C<sub>3</sub>N<sub>4</sub> Composite Photocatalyst and Its Enhanced Visible Light Photocatalytic Degradation of Amido Black 10b. *Sep. Purif. Technol.* **2019**, *210*, 125–134. [\[CrossRef\]](#)
34. Qin, H.; Guo, R.T.; Liu, X.Y.; Pan, W.G.; Wang, Z.Y.; Shi, X.; Tang, J.Y.; Huang, C.Y. Z-scheme MoS<sub>2</sub>/g-C<sub>3</sub>N<sub>4</sub> Heterojunction for Efficient Visible Light Photocatalytic CO<sub>2</sub> Reduction. *Dalton Trans.* **2018**, *47*, 15155–15163. [\[CrossRef\]](#) [\[PubMed\]](#)
35. Shi, X.W.; Fujitsuka, M.; Kim, S.; Majima, T. Faster Electron Injection and More Active Sites for Efficient Photocatalytic H<sub>2</sub> Evolution in g-C<sub>3</sub>N<sub>4</sub>/MoS<sub>2</sub> Hybrid. *Small* **2018**, *14*, 9. [\[CrossRef\]](#) [\[PubMed\]](#)
36. Kumaresan, N.; Sinthiya, M.M.A.; Sarathbavan, M.; Ramamurthi, K.; Sethuraman, K.; Babu, R.R. Synergetic Effect of g-C<sub>3</sub>N<sub>4</sub>/ZnO Binary Nanocomposites Heterojunction on Improving Charge Carrier Separation through 2D/1D Nanostructures for Effective Photocatalytic Activity under The Sunlight Irradiation. *Sep. Purif. Technol.* **2020**, *244*, 116356. [\[CrossRef\]](#)
37. Ji, H.; Du, P.; Zhao, D.; Li, S.; Sun, F.; Duin, E.C.; Liu, W. 2D/1D Graphitic Carbon Nitride/Titanate Nanotubes Heterostructure for Efficient Photocatalysis of Sulfamethazine under Solar Light: Catalytic “Hot Spots” at the Rutile–Anatase–Titanate Interfaces. *Appl. Catal. B Environ.* **2020**, *263*, 118357. [\[CrossRef\]](#)
38. Tan, Y.G.; Shu, Z.; Zhou, J.; Li, T.T.; Wang, W.B.; Zhao, Z.L. One-step Synthesis of Nanostructured g-C<sub>3</sub>N<sub>4</sub>/TiO<sub>2</sub> Composite for Highly Enhanced Visible-Light Photocatalytic H<sub>2</sub> Evolution. *Appl. Catal. B Environ.* **2018**, *230*, 260–268. [\[CrossRef\]](#)



- 
39. Ohsaka, T.; Izumi, F.; Fujiki, Y. Raman spectrum of anatase TiO<sub>2</sub>. *J. Raman Spectrosc.* **1978**, *7*, 321–324. [[CrossRef](#)]
  40. Martin, D.J.; Qiu, K.; Shevlin, S.A.; Handoko, A.D.; Chen, X.; Guo, Z.; Tang, J. Highly Efficient Photocatalytic H<sub>2</sub> Evolution from Water Using Visible Light and Structure-Controlled Graphitic Carbon Nitride. *Angew. Chem. Int. Ed.* **2014**, *53*, 9240–9245. [[CrossRef](#)]
  41. Wu, P.; Wang, J.; Zhao, J.; Guo, L.; Osterloh, F.E. Structure Defects in g-C<sub>3</sub>N<sub>4</sub> Limit Visible Light Driven Hydrogen Evolution and Photovoltage. *J. Mater. Chem. A* **2014**, *2*, 20338–20344. [[CrossRef](#)]
  42. Liu, H.; Zhang, Z.-G.; He, H.-W.; Wang, X.-X.; Zhang, J.; Zhang, Q.-Q.; Tong, Y.-F.; Liu, H.-L.; Ramakrishna, S.; Yan, S.-Y.; et al. One-step Synthesis Heterostructured g-C<sub>3</sub>N<sub>4</sub>/TiO<sub>2</sub> Composite for Rapid Degradation of Pollutants in Utilizing Visible Light. *Nanomaterials* **2018**, *8*, 842. [[CrossRef](#)] [[PubMed](#)]
  43. Wu, M.-C.; Wu, P.-Y.; Lin, T.-H.; Lin, T.-F. Photocatalytic Performance of Cu-doped TiO<sub>2</sub> Nanofibers Treated by The Hydrothermal Synthesis and Air-thermal Treatment. *Appl. Surf. Sci.* **2018**, *430*, 390–398. [[CrossRef](#)]